UNIVERSITY OF TWENTE.

Faculty of Electrical Engineering,
Mathematics & Computer Science
Faculty of Engineering Technology

Modeling The JLO Exoskeleton and Designing a Controller for Gait Entrainment

Grace C. Iroagalachi
Master's Thesis
March 2025

Supervisors:
M.K. MacLean, Phd
dr.ir. A.Q.L. Keemink

Graduation committee:
prof.dr.ir. H. van der Kooij
dr.ir. R.G.K.M. Aarts

Neuromechanical Engineering (ET-BE-NE)
Faculty of Mechanical Engineering,
University of Twente
P.O. Box 217
7500 AE Enschede
The Netherlands

Abstract

Gait entrainment occurs when a human synchronizes the period of their gait cycle to the period of an external, rhythmic input. Gait entrainment can be done with an ankle exoskeleton; the exoskeleton delivers small torque pulses to the human ankle provoking a subconscious adaptation of gait cadence.

Researchers from the Neuromuscular Robotics research group at the University of Twente use the JLO, a lower limb exoskeleton, to study gait entrainment. The JLO's current controller was designed using model-free techniques, and provides sub-standard torque tracking, severely limiting the ability to investigate gait entrainment. Therefore, the goal of this thesis is to create a model of the exoskeleton that facilitates controller design, and to use that model in designing a controller that minimizes the error between the desired torque pulses and the measured pulses.

To this end, the JLO is modeled as a nonlinear system. The combination of feedback linearizing control and feedforward control results in a lower root mean square error (RMSE) than the JLO's current, model-free controller. Simulation experiments showed that when tracking torque pulses, the proposed controller has an RMSE of 0.6361 Nm, while the current controller has an RMSE of 0.7368 Nm. The feedback linearizing controller thus improves the current torque tracking capabilities of the JLO exoskeleton, and better facilitates the study of gait entrainment as a rehabilitative strategy.

Summary

The JLO is a lower-limb ankle exoskeleton that can be used to apply torque pulses to the ankle. Torque pulses are a method to incite gait entrainment during walking, so the ability to apply consistent pulses is a prerequisite for gait entrainment studies. The quality of the torque pulses supplied by the exoskeleton is partly determined by the exoskeleton's controller, and the torque tracking of the JLO's current controller left room for improvement. The current controller is the product of model-free controller design, so the goal of this thesis was to explore any improvements in torque tracking offered by model-based controller design.

In service of modeling the JLO, this thesis coupled a transfer function that describes the closed-loop motor dynamics, to a nonlinear model of the spring force transmitted from the motor to the ankle via a Bowden cable. Characterization of the motor's closed dynamics revealed limits on the motor's velocity and acceleration which was another factor affecting torque tracking. In spite of these limitations, simulations showed that combining a feedforward controller with a feedback linearizing controller resulted in a root mean square of 0.6361 Nm when tracking torque pulses with a magnitude of 10 Nm. The error of the new controller is lower than that of the current feedback controller, which is 0.7368 Nm.

While The JLO model presented in this thesis was sufficient for controller design, future iterations of the model should focus on experimental validation of the designed controller, and on expanding the JLO model to more accurately portray the friction and hysteresis present in the Bowden cable.

Contents

Chapter 1

Introduction

At 70 years, the global average life expectancy in 2021 is more than double what it was in 1900 [1]. Accompanying this increase in life expectancy is an increase in the prevalence of abnormal gait patterns, as age-related diseases often present with a degradation of gait characteristics. Aging predisposes us to neurodegenerative disorders, e.g., Parkinson's disease, and these disorders often present with an increased variability in gait parameters [2].

The importance of rehabilitation for gait disorders cannot be overstated; rehabilitation improves autonomy, and the quality of life of the patients [3]. Whereas past rehabilitative techniques demanded the continuous intervention of a physiotherapist, there is currently a pivot towards robot-assisted rehabilitative strategies. Robot-assisted rehabilitative strategies have experienced an uptick because they reduce the physical strain on the physiotherapist, and they can better guarantee the repeatability of the exercises [4].

A potential form of robot-assisted rehabilitation is cueing. Cueing is the use of external stimuli, like tactile vibrations or a metronome, to aid movement continuity [5]. Sejdic et al. [6] showed that auditory cues reduced stride interval variability in fifteen healthy participants, and [7] hypothesized that rhythmic auditory stimulation improved the gait velocity, cadence, and stride length of nineteen patients with idiopathic Parkinson's disease.

Cueing has thus been proposed as a way of tackling gait disorders because human locomotion is susceptible to entrainment; entrainment being the human capacity to synchronize our movement with an external, rhythmic stimuli [8]. Ahn et al. [9] showed that subjects modulated their gait frequency untill it coincided with the frequency of a series of plantarflexion torque pulses applied at the ankle. Regardless of the gait phase in which the torque pulses were first applied, in entrained gait, the torque pulses occurred at a point in the gait phase where they assist ankle push-off [10].

1.1 Motivation

Similar to [9], the mechanism for instigating entrainment in this thesis is a series of plantarflexion torque pulses applied at regular intervals to the ankle. The pulses are designed have a period that is 25–50 ms shorter than a person's average stride duration; the idea being that a person will modify their walking such that their gait cycle has the same period as that of the torque pulses.

Accurate, and repeatable experiments on gait entrainment require a lower limb exoskeleton that can deliver torque pulses at any point in the gait cycle. In [11], torque pulses that have a trapezoidal shape as depicted in Figure 1.1 were applied using the JLO, which is a lower-limb exoskeleton developed at the University of Twente [12]. The exoskeleton is shown in Figure 1.2. The exoskeleton was designed to be lightweight, robust and capable of supporting users during dynamic movements like walking, running, and jumping. The exoskeleton is able to provide up to 20 Nm of plantarflexion torque to the user, and the controller has a bandwidth of 8 Hz [12].

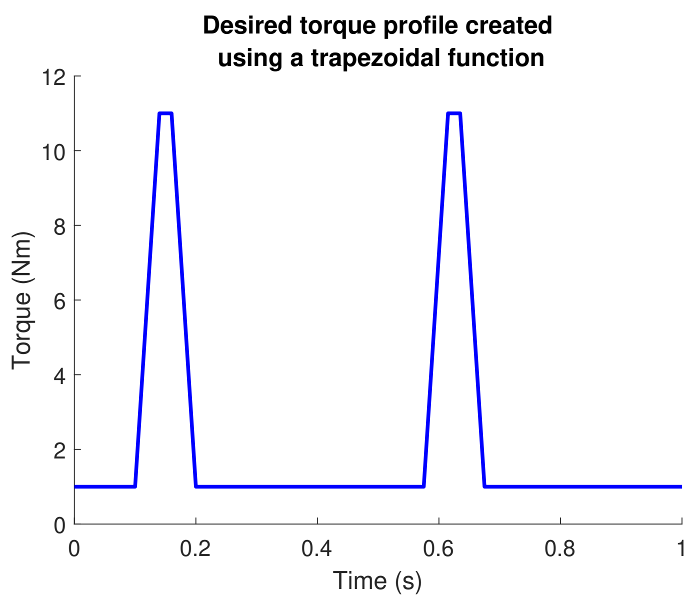

Figure 1.1: A series of the desired torque pulses to be applied to the ankle. The torque pulses have a trapezoidal shape.

Figure 1.2: A participant wearing the JLO exoskeleton on their right foot [11].

Exoskeletons such as the JLO typically have a low-level and a high-level controller. The high-level controller determines the torque to be sent to the exoskeleton, and the low-level controller enforces the torque demanded by the high-level controller. The low-level controller most commonly used with the JLO is the PD* controller proposed by Zhang et al [13]. The controller's proportional term acts on the error between the desired torque and the measured torque, but the derivative term acts on the motor velocity, instead of the derivative of the torque error. The PD* controller was designed using model-free techniques which entailed tuning the controller gains untill the system response was deemed satisfactory.

Mahdian et al. [11] studied the JLO's ability to deliver torque pulses during all phases of the gait cycle. Per their research, combining the PD* controller with the iterative learning controller proposed by [13] improved the torque tracking root mean square error (RMSE) of the JLO from 3.5 Nm to 2 Nm [11]. Zhang et al. [13], however, reported an RMSE of 0.57 Nm when the PD* controller was used with an iterative learning controller.

Furthermore, although combining the iterative learning controller with the PD* controller improved torque tracking compared to only the PD* controller, the improvement is not consistent for all phases of the gait cycle. Torque tracking in periods of high ankle velocity, like early stance or ankle push off, remain suboptimal [11]. Mahdian et al. [11] ascribed this discrepancy in RMSE to the velocity limits of the JLO's actuator.

Besides the velocity limits, the JLO's inability to consistently deliver torque pulses might be an issue with the controller bandwidth, or the exoskeleton setup. This thesis is thus born out of the need to delineate the JLO's frictional and elastic characteristics, in a bid to improve the system's torque tracking.

1.2 Research goals

The goal is to create a controller for the JLO using model-based techniques for controller design. The following sub questions will aid in accomplishing this goal:

1. What is a competent model for the motor dynamics?
2. What is a competent model for the stiffness of the system?
3. How can the friction in the system be modeled?
4. What are the factors limiting the magnitude of torque pulses that the JLO can deliver?
5. How can the controller compensate for the load-side disturbance induced by the wearer?

1.3 Report organization

The subsequent sections of this thesis provide more information about the modeling and control system design process. Chapter 2 details the equations that describe the exoskeleton and motor dynamics. The process of identifying the transfer function from the desired motor velocity to the actual motor velocity is presented in Chapter 3. Chapter 4 is about the process for identifying the stiffness characteristics of the system. Chapter 5 delves into the design of a feedback linearising controller and compares it to the current PD* controller, and this thesis is rounded off with a discussion of the research in Chapter 6, and a conclusion in Chapter 7.

Chapter 2

Modeling the JLO

Figure 2.1 illustrates the exoskeleton setup, and how the individual components are assembled. The exoskeleton consists of a shank frame which is connected to a foot frame with a set of ball bearings whose location approximates the ankle's axis of rotation in the sagittal plane. The exoskeleton provides a plantar-flexion torque around the ankle by pulling the Bowden cable upwards [14].

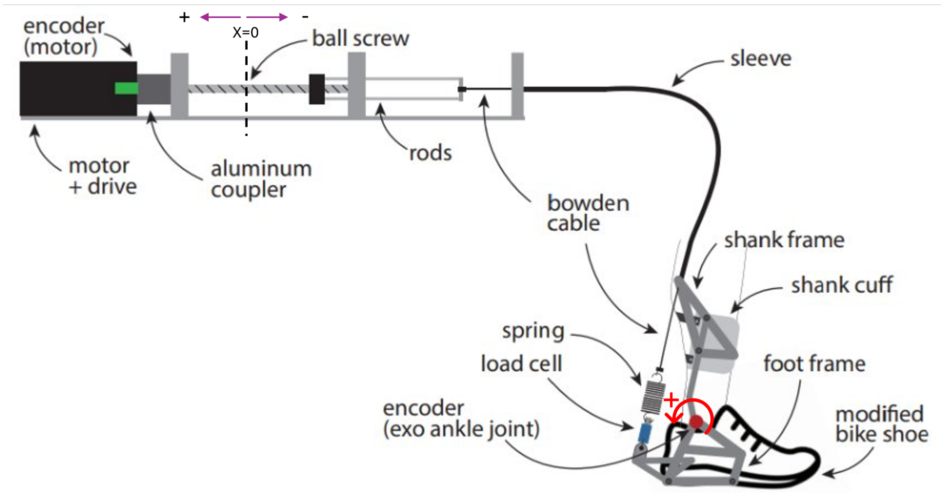

Figure 2.1: Schematic of the ankle exoskeleton [14]. The directions for positive motion of the ball screw and positive rotation of the ankle are indicated by the purple-, and red-colored arrows respectively.

Moog's SMB82 motor powers the exoskeleton, and an aluminum coupler connects the motor to the Misumi ball screw. The ball screw transmission is used to convert rotary motion to linear motion. The ball screw pulls the Bowden cable by way of two aluminum rods that slide through an aluminum block. The Bowden cable is in series with a spring which is connected to the foot frame of the exoskeleton.

The exoskeleton is equipped with a loadcell to measure the force transmitted by the Bowden cable, and an absolute magnetic encoder measures the exoskeleton angle. The motor has current sensors from which the motor torque can be calculated, and an encoder to provide position and velocity information. Real-time control of the exoskeleton is facilitated by the EtherCAT protocol that is used to connect the motor and exoskeleton. Signals are sent and received via the TwinCAT software user interface.

2.1 Equations of motion for the exoskeleton

Figure 2.2 shows an ideal physical model of the exoskeleton system. The equations of motion are derived from the ideal physical model. Table 2.1 explains the variables and parameters that appear in Figure 2.2, and in the equations of motion.

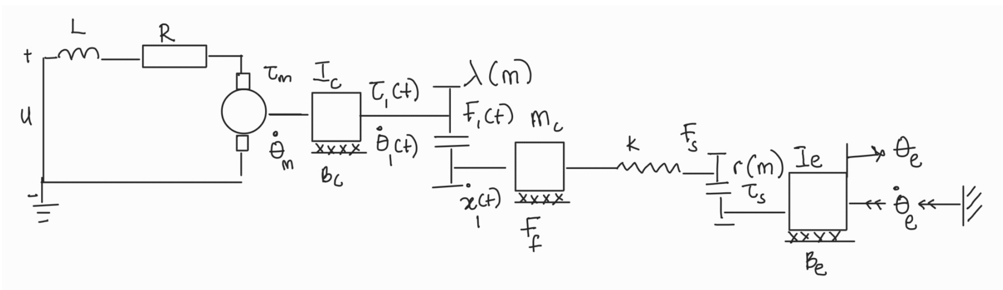

Figure 2.2: Ideal physical model showing the electromechanical domain of the exoskeleton.

The ball screw has a transmission ratio of λ (m). On the left hand side of the screw transmission, the torque input, τ_1 is given by:

$$\tau_1(t) = \tau_m(t) - I_c\ddot{\theta}_m(t) - B_c\dot{\theta}_m(t) \tag{2.1}$$

$$\theta_1(t) = \theta_m(t). \tag{2.2}$$

The spring, inertial, frictional, and gravitational forces on the right hand side of the screw transmission are reflected to a point before the screw transmission:

$$\tau_1 = \lambda F_1 = \lambda \left[m_c \left(r\ddot{\rho}(t) - \lambda\ddot{\theta}_m(t)\right) + F_s(t) + m_c g + F_f(t)\right]. \tag{2.3}$$

$$\tau_m(t) = I_c\ddot{\theta}_m(t) + B_c\dot{\theta}_m(t) + \lambda\left(m_c\left(\lambda\ddot{\theta}_m(t) - r\ddot{\theta}_e(t)\right) + F_s + m_c g + F_f(t)\right) \tag{2.4}$$

Equation 2.4 is the combination Equations 2.1, 2.2, and 2.3 rewritten so that the motor torque is on the left hand side. Furthermore, the equation of motion for the right hand side of the exoskeleton joint is:

$$I_e\ddot{\theta}_e + B_e\dot{\theta}_e = \tau_s. \tag{2.5}$$

Lastly, the electrical dynamics of the motor are summarized by the following equations [15]:

$$u(t) = L\dot{i}(t) + Ri(t) + K_e\dot{\theta}_m(t) \tag{2.6}$$

$$\tau_m(t) = K_t i(t). \tag{2.7}$$

Table 2.1: Important parameters for describing the equations of motion of the exoskeleton.

	Symbol	Description	Value	Unit
1	λ	Screw transmission ratio	$\frac{0.005}{2\pi}$	m
	K_e	Back electromotive force constant	0.23	Vs
	K_t	Torque constant	0.40	$\frac{\text{Nm}}{\text{A}}$
	L	Stator inductance	1.5190	H
	R	Stator resistance	0.9268	Ohm
	g	Gravitational constant	9.81	ms^{-2}
2	I_c	Inertia of motor & screw transmission		kgm^2
	m_c	Mass of spring & Bowden cable		kg
	B_c	Damping coefficient of motor & screw transmission		$\frac{\text{Nms}}{\text{rad}}$
	I_e	Inertia of the shoe		kgm^2
	B_e	Damping coefficient of the exoskeleton		$\frac{\text{Nms}}{\text{rad}}$
3	τ_m	Motor torque		Nm
	θ_m	Motor position		rad
	θ_e	Exosketon joint angle		rad
	F_f	Bowden cable friction		N
	τ_1	Torque input to the screw transmission		Nm
	F_1	Force output of the screw transmission		N
	τ_s	Torque measured by the spring		Nm
	u	Voltage supplied to the motor		V
	i	Motor current		A
	r	Exoskeleton moment arm		m

Categories 1 and 2 of Table 2.1 contain the known and unknown parameters of the system, while category 3 contains the system variables. System identification demands that a model be substituted to describe the elastic- and frictional behavior of the system. Therefore Chapters 3, and 4 focus on models to describe the motor behavior, and identifying the elastic properties of the system respectively. The friction is discussed in Appendix **??**.

Chapter 3

Identification of the Motor's Closed-Loop Dynamics

The motor has a maximum velocity of 7500 rpm, but has a safety limit of 6000 rpm that is implemented in the software. The screw transmission endstops further limit the motor position to between -40–90 rad. Disconnecting the motor from the screw transmission eliminated these limits for the identification process.

Figure 3.1 shows a simplified block diagram of the motor from the desired motor velocity, $\dot{\theta}_{m,\text{des}}$ to the actual motor velocity, $\dot{\theta}_m$. The input to the velocity controller is the error between the velocity setpoint and the actual velocity, $e_{\dot{\theta}_m}$. The feedback velocity controller determines the desired current, i_{des}.

The error between the desired current and the actual current, e_i, is fed to the feedback current controller. The applied voltage V is the output of the current controller, and is summed with the counter-electromotive voltage which is given by $K_e\dot{\theta}_m(t)$ in Equation 2.6. The result of this summation is the input to the transfer function, $H_{i/V}$, which captures the relationship between the voltage and the motor current. The motor torque τ_m is determined from the current using Equation 2.7. The transfer function $H_{\ddot{\theta}/\tau}$ relates the motor torque to the motor acceleration $\ddot{\theta}$, and the motor velocity is obtained by integrating the acceleration.

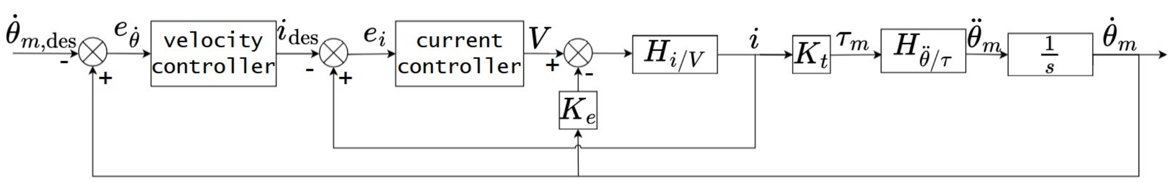

Figure 3.1: Depiction of the signal flow from the desired motor velocity to the actual motor velocity.

Wyeth [16] posits that treating the motor as a velocity source, as suggested by Robinson [17], can assure good torque control, even in the presence of friction losses. A well-tuned velocity controller should be able to handle low-frequency torque disturbances, and the series elastic element decouples high-frequency torque disturbances at the load side [16]. The motor is thus considered a velocity source, and the next section details the identification of the transfer function from the desired velocity to the actual velocity.

3.1 Process for identifying the motor velocity transfer function

The motor is controlled in velocity mode so only velocity commands could be sent to the motor. The motor was excited with step signals, and each step input lasted 0.2 seconds. Figure 3.2 shows an example of the step command sent to the motor. The experiment was repeated for 17 velocities ranging from 10 rpm, up to and including 7000 rpm.

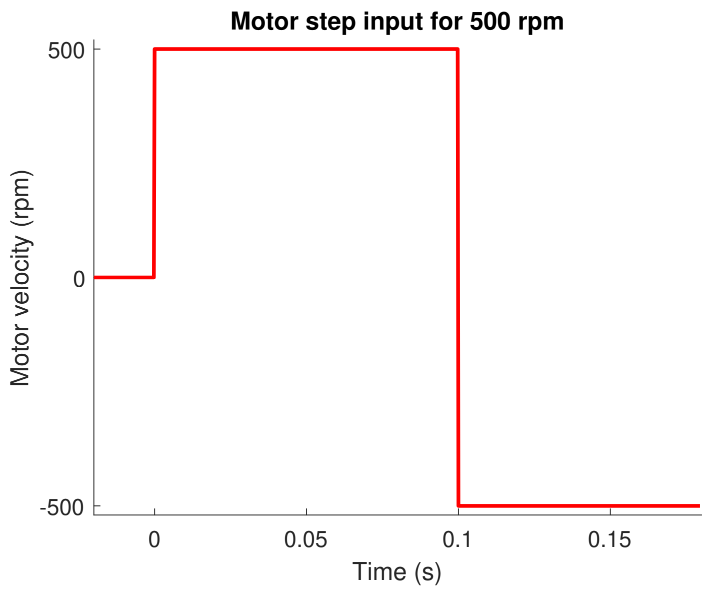

Figure 3.2: Example of step input commanded to the motor velocity controller.

The data were sampled at 4000 Hz. The collected velocity signals were divided into 3 segments to which a Hanning window was applied. The system in Figure 3.1 is lumped into one closed-loop transfer function for the identification process. The data were used to estimate the nonparametric frequency response function using the estimator

$$\hat{H}_f = \frac{S_{\text{yu}}}{S_{\text{uu}}}, \tag{3.1}$$

where

$$S_{\mathsf{yu}} = \frac{1}{N}\mathcal{F}(\dot{\theta}_m)\mathcal{F}(\dot{\theta}_{m,\mathsf{des}}) \tag{3.2}$$

and

$$S_{\mathsf{uu}} = \frac{1}{N}\mathcal{F}(\dot{\theta}_{m,\mathsf{des}})\mathcal{F}(\dot{\theta}_{m,\mathsf{des}}). \tag{3.3}$$

$\mathcal{F}(\cdot)$ denotes the fast Fourier transform the time-domain-based data.

A 2nd or a 3rd order transfer transfer function are candidate models for fitting the nonparametric frequency response function to a parametric model. The 2nd order transfer function is represented by

$$\hat{H}_t(s) = \frac{s+\omega_n^2}{s^2+2\zeta\omega_n s+\omega_n^2}, \tag{3.4}$$

where ζ is the damping ratio, and ω_n is the natural frequency. The actuator could have higher order dynamics hence the benefits of the 3rd order below will also be investigated.

$$\hat{H}_t(s) = \frac{s^2+(\omega_n^2 p+2\zeta\omega_n p)s+\omega_n^2 p}{(s+p)(s^2+2\zeta\omega_n s+\omega_n^2 p)}, \tag{3.5}$$

Assuming that the motor transfer function has the form of the 2nd order system given in Equation 3.4 allows initial values for the estimation of the parameters ζ, and ω to be obtained from the step response plots [18]. Both parameters are generated as follows:

The peak overshoot, M is

$$M = \frac{\dot{\theta}_{\mathsf{max}} - \dot{\theta}_{\mathsf{ss}}}{\dot{\theta}_{\mathsf{ss}}}, \tag{3.6}$$

where $\dot{\theta}_{\mathsf{max}}$ is the peak value attained by the motor actual velocity, and $\dot{\theta}_{\mathsf{ss}}$ is the velocity when the motor reaches its steady state. The damping ratio is determined from the percentage overshoot in the following way:

$$\zeta = \sqrt{\frac{\ln^2 M}{\ln^2 M+\pi}}. \tag{3.7}$$

The damped frequency ω_d is a measure of how fast the system is oscillating, and is estimated from the step response. The natural frequency ω_n is determined from the damped frequency as given below:

$$\omega_n = \frac{\omega_d}{\sqrt{1-\zeta^2}} \tag{3.8}$$

MATLAB's lsqnonlin optimization function was used to determine the parameters ω_n, ζ, and p, using the initial guesses, and the following cost function:

$$V = \frac{1}{N}\sum_{i=1}^{N}\left(\frac{1}{\sqrt{f_i}}\gamma_i^2\left|\ln\left(\frac{\hat{H}_f(f_i)}{\hat{H}_t(f_i)}\right)\right|\right)^2, \tag{3.9}$$

where N is the number of data points, f are the frequencies, and $\gamma^2(f)$ is the coherence and can be calculated as follows:

$$\gamma^2(f_i) = \frac{|S_{\text{yu}}(f_i)|^2}{S_{\text{yy}}(f_i)S_{\text{uu}}(f_i)}. \tag{3.10}$$

The coherence gives an indication if two signals are linearly related, and weighting the cost function by the coherence emphasizes the reliable frequencies. Furthermore, Equation 3.9 is also weighted by $\frac{1}{\sqrt{f}}$ to compensate for the comparative sparsity of data points in the low frequency region compared to the high frequency region of the logarithmic frequency axis.

3.2 Results of the motor identification process

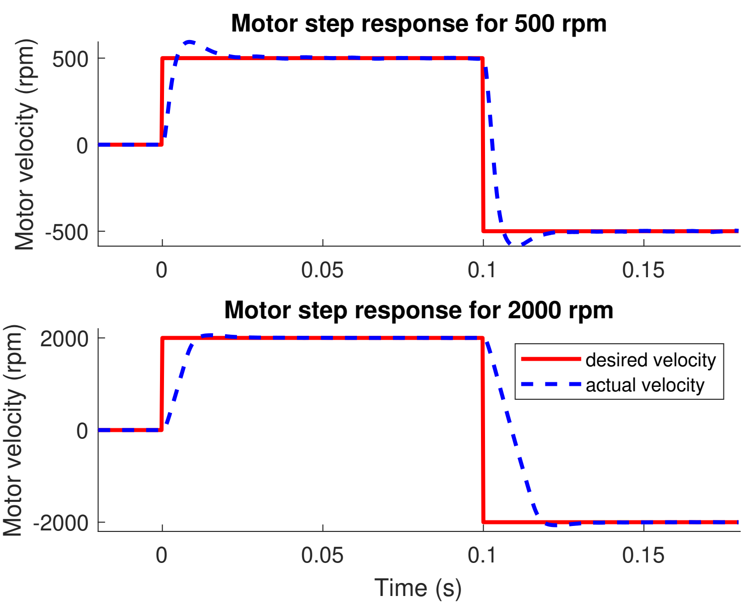

Figure 3.3: Step response of the motor for a command of 500 rpm and 2000 rpm.

Figure 3.3 shows an example of the motor's step response to velocity commands of 500 rpm and 2000 rpm. The motor step responses show the presence of an acceleration limit, and Figure 3.4 shows that the motor acceleration plateaus after 2000 rpm. The motor acceleration for each of the step input is defined as the slope of the step response for velocities between 10% and 50% of the commanded value.

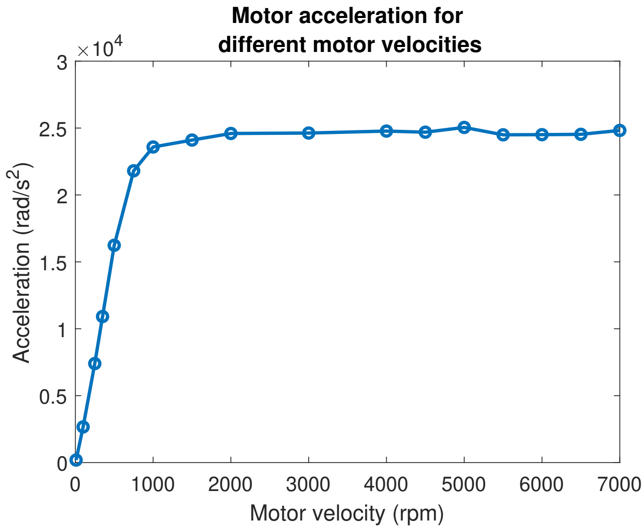

Figure 3.4: Acceleration limits for the commanded velocity step input.

Taking the average of the slew rates for all velocities from 2000 rpm to 7000 rpm reveals the acceleration limit of 24678 rad/s^2. In the presence of this acceleration limit, only the step response data for 100, 250, 350, 500, 750 rpm were used in the estimation of the motor velocity transfer function. The peak overshoot, $M = 18.3\%$. The damping ratio, ζ is 0.691. The damped frequency ω_d is 65 Hz, making the natural frequency ω_n 71.48 Hz.

Figure 3.5 shows the results of the transfer function identification process. The responses of the 2nd, and 3rd order models are overlapping. The fit error is the mean square error as given in Equation 3.9. With a fit error of 8.5021 $\cdot$ 10^{-4}, the 3rd order model narrowly outperforms the 2nd order model which has a fit error of 8.5084 $\cdot$ 10^{-4}. The error is based on the frequency response of the parametric and nonparametric models, and has no unit. The chosen transfer function is the 2nd order model given by:

$$\frac{s + 3.993 \cdot 10^5}{s^2 + 666.9s + 3.993 \cdot 10^5}.$$

The step response plot of both the 2nd order, and the 3rd order models further validate the choice of the second order model. Figure 3.6 shows an overlap between response of the 2nd order transfer function in blue, and the 3rd order model in black. The 2nd order model is less complex than the 3rd order model, and is henceforth used in simulating the motor closed-loop dynamics.

Alongside the position and velocity limits, the acceleration limit is included in the motor model by converting the transfer function in Equation 3.2 from the frequency domain to the time domain as given below:

$$\dddot{\theta}_m = \text{sat}(\ddot{\theta}_{m,\text{des}}) + 3.993 \cdot 10^5 \dot{\theta}_{m,\text{des}} - 666.9\ddot{\theta}_m - 3.993 \cdot 10^5 \dot{\theta}_m. \tag{3.11}$$

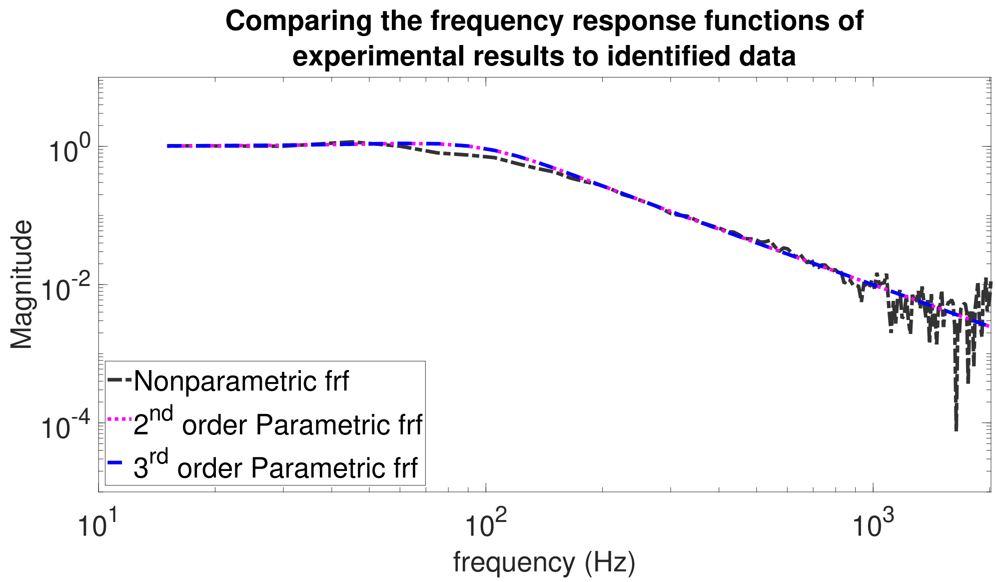

Figure 3.5: Bode magnitude plot of the 2nd-, and 3rd order transfer function models.

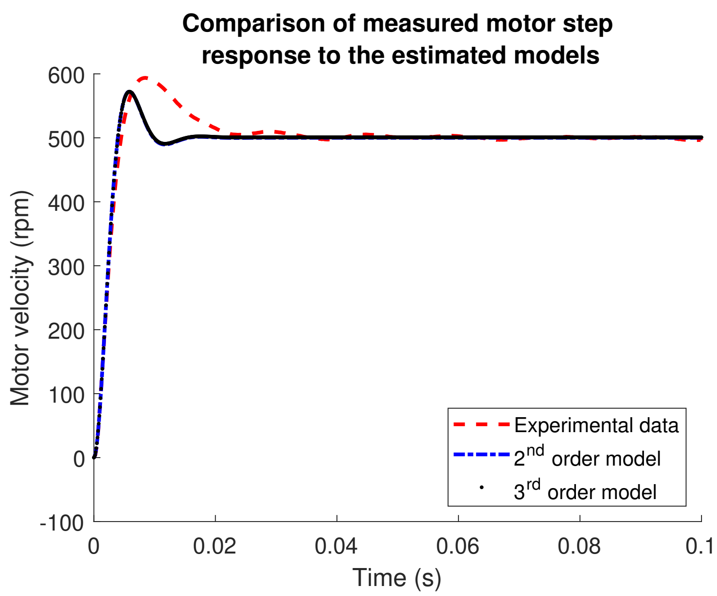

Figure 3.6: The motor velocity in response to a step input of 500 rpm.

3.3 Discussion of the motor closed-loop dynamics identification process.

The initial guesses for ζ, and ω_n were generated using only the step response for a step input of 500 rpm, whereas the identification of the motor's closed loop transfer function was done using the step response data for 100, 250, 350, 500, and 750 rpm. It is possible that averaging the values of ζ and ω_n for all 5 step responses would yield a more accurate result. However, the log loss function in Equation 3.9 is convex so the parameters are found at the global minimum regardless of the initial guess.

The nonparametric frequency response function was used to estimate the transfer function from desired motor velocity to actual motor velocity. The 2nd and 3rd order models were suggested because the motor step responses showed oscillatory behavior indicating a 2nd order system at minimum. Also, the nonparametric frequency response function showed a roll-off of 10/decade which indicates a system that behaves like an integrator in the high frequency region, i.e., the system transfer function has a relative degree of 1.

Adding more parameters in the 3rd order model provides more leeway to capture dynamics like vibrations or time delays. However, the 2nd order transfer function was chosen over the 3rd order model because the 2nd order model is less complex than the third order model. As both models have similar fit errors, choosing the 2nd does not sacrifice a better fit for simplicity.

Both models do not completely describe the actual motor response. From Figure 3.6, it is obvious that the estimated models do not have as much overshoot as the actual system. The estimated damping ratio is 0.7852 compared to the initial guess of 0.691 determined in Equation 3.7. A higher damping ratio of course translates to less overshoot.

The imperfect fit of both models could be due to the literal implementations of Equations 3.4 and 3.5 during the nonlinear optimization. Lumping the parameters ζ, ω_n, and p reduced the number of parameters available to fit the data, and could be a reason for the model underfitting the data. Despite this deficiency, the parametric model captures the motor's response time and steady state value. In combination with the low fit error, the parametric model is a competent model of the actuator.

The motor has a rotor inertia of $1.4 \cdot 10^{-4}$ kgm^2. With a stall torque of 3 Nm, the expected acceleration limit is 21429 rad/s^2. The experimentally-determined motor acceleration, however, is 24678 rad/s^2. The source of the discrepancy in the acceleration limits is currently unclear, and could be due to errors in current measurements or incorrect information in the motor datasheet. For the simulation experiments in Chapter 5, the motor acceleration is set to 24678 rad/s^2.

Chapter 4

Identification of the Stiffness Properties

The exoskeleton is powered by a series elastic actuator, making it imperative to first understand the elastic behavior of the actuator, before moving on to controller design. A series elastic actuator is an actuator that has an elastic component, like a spring, in the drive train between the motor and the load. Springs are often modeled using Hooke's law, but Bowden cables are notorious for their nonlinear behavior [15]. As the JLO has a spring in series with a Bowden cable in the drivetrain, the next section details nonlinear mathematical models to describe the force transmission of the JLO exoskeleton. Unlike in Chapter 3, the motor is connected to the exoskeleton during the identification process, and system here refers to the JLO as illustrated in Figure 2.1.

4.1 Process for the identification of the system stiffness

Possible mathematical functions for fitting the shape of the JLO's force-displacement plot include a polynomial function and a power law function. These models are motivated by preliminary experiments on the JLO that reveal a system rife with slack and hysteresis as shown in Figure 4.1.

The slack is evidenced by the minimal change in the spring force for motor positions between 0 and approximately 4 rad. Slack behavior occurs because the motor must first rotate to pull the Bowden cable taut before the spring can deflect. Furthermore, it is apparent that the force behaves differently when the motor velocity is positive and the Bowden cable is pulled by the motor, and when the motor velocity is negative and the Bowden cable is released.

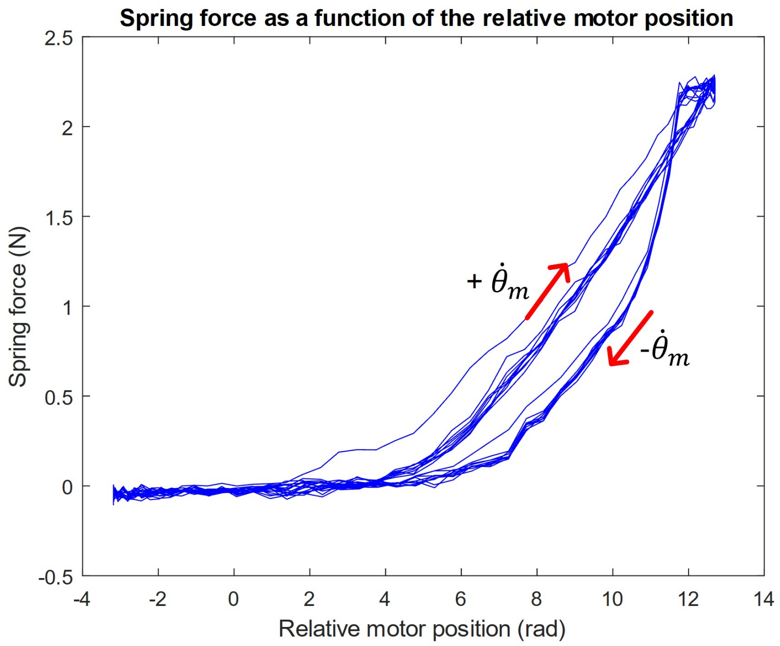

Figure 4.1: Force-displacement relation when the exoskeleton is actuated by the motor. Here, the exoskeleton's ankle joint did not serve as an input, and the spring deflection is purely due to the motor's motion.

The proposed polynomial model for the torque transmitted from the motor via the Bowden cable is

$$F_{s,\mathrm{m}} = \begin{cases} k_{\mathrm{m},1}(\lambda\theta_m) + k_{\mathrm{m},2}(\lambda\theta_m)^2 + k_{\mathrm{m},3}(\lambda\theta_m)^3 + k_{\mathrm{m},4}(\lambda\theta_m)^4 \\ +k_{\mathrm{m},5}(\lambda\theta_m)^5 \quad \text{if } \theta_m > 0, \\ 0 \text{ otherwise.} \end{cases} \tag{4.1}$$

Similarly, the polynomial model for the load-side torque disturbance from a person wearing the exoskeleton is

$$F_{s,\mathrm{e}} = \begin{cases} k_{\mathrm{e},1}(r\theta_e) + k_{\mathrm{e},2}(r\theta_e)^2 + k_{\mathrm{e},3}(r\theta_e)^3 + k_{\mathrm{e},4}(r\theta_e)^4 \\ +k_{\mathrm{e},5}(r\theta_e)^5 \quad \text{if } \theta_e > 0, \\ 0 \text{ otherwise.} \end{cases} \tag{4.2}$$

$k_{\mathrm{m},n}$, and $k_{\mathrm{e},n}$ are stiffness coefficients with units N/m^n. θ_m, and θ_e are the motor and exoskeleton positions respectively, in rad. λ is the transmission ratio of the ball screw in m, and r is the moment arm in m.

The power law model for the torque supplied by the motor is

$$F_{s,\mathrm{m}} = \begin{cases} k_{\mathrm{m}}(\lambda\theta_m)^{p_m} \quad \text{if } \theta_m > 0, \\ 0 \text{ otherwise.} \end{cases} \tag{4.3}$$

The power law model for the load-side torque disturbance from the human is

$$F_{s,\mathrm{e}} = \begin{cases} k_{\mathrm{e}}(r\theta_e)^{p_e} & \text{if } \theta_e > 0, \\ 0 \text{ otherwise.} \end{cases} \tag{4.4}$$

k_{m}, and k_{e} are stiffness coefficients with units N/m^{p_i}, where p_i is the exponent of the power law.

The polynomial models are functions of the regressors θ_{m}, or θ_{e}, and the coefficients in the polynomial model are determined using linear least squares regression. The parameters in the power law function are determined using MATLAB's *fmincon* function for nonlinear optimization. The results of the polynomial models informed the initial guesses for the parameters in the power law. Furthermore, the cost function used for the optimization is the mean squared error between the predicted spring torque and the measured spring torque. The cost function used for the optimization is

$$W(\theta_m) = \frac{1}{N}\sum_{n=1}^{N} (\tau_s - \hat{\tau}_s)^2, \tag{4.5}$$

where N is the number of data points used for the estimation. The estimated spring torque, $\hat{\tau}_s$, is the summation of the torque transmitted from the motor, and the torque contribution of a person wearing the exoskeleton,

$$\hat{\tau}_s = r\left(F_{s,\mathrm{m}} - F_{s,\mathrm{e}}\right). \tag{4.6}$$

Common pitfalls associated with model fitting using optimization routines include the risk of overfitting, and in the case of gradient descent algorithms, a risk that the solution arises from a local minimum as opposed to a global one. To tackle overfitting, the data was split into 5 folds; 4 folds served as the training data and 1 fold as the test data. This is known as k-fold cross validation [19]. The chance of the solution arising from a local minimum instead of a global one is minimized by using the mean squared error cost function in Equation 4.5. The mean square error is a convex function and has one global minimum.

For the stiffness identification, zeroing of the JLO's load cell, exoskeleton position, and motor position was done according to [12] prior to all experiments. All data were sampled at 1000 Hz and filtered in both the forward and reverse directions with a 2$^{\text{nd}}$ order low-pass filter. The filter cutoff frequency is 100 Hz, and the filter coefficients are given below:

$$H(z) = \frac{0.0675 + 0.1349z^{-1} + 0.0675z^{-2}}{1.0000 - 1.1430z^{-1} + 0.4128z^{-2}}.$$

Experiment 1: Motor-side stiffness

Sinusoidal velocity signals centered at 0 and with amplitudes of 0.5, 1, 2, and 5 rad/s were commanded to the motor. The motor was also excited with constant velocity signals with amplitudes of 0.1, 0.2, 0.5, 1, 2, 5, 10 rad/s. The dummy foot in Figure 4.2 served to keep the exoskeleton upright during the experiments. With only the motor contributing to the spring deflection, $F_{s,\mathrm{e}} = 0$.

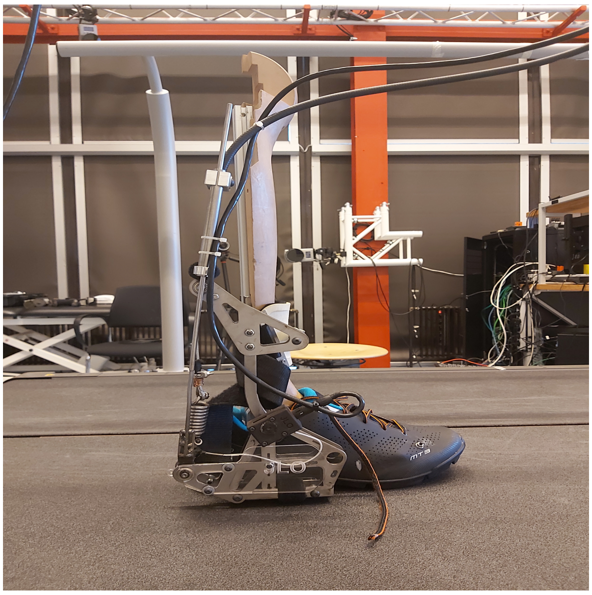

Figure 4.2: Positioning of the exoskeleton during experiments to determine the motor-side stiffness.

Experiment 2: Load-side stiffness

For the load-side influence on the measured spring torque, a participant walked on a treadmill while wearing the JLO on their right foot . The participant walked for 183 s with a treadmill speed of 1.2 m/s, for 220 s with a treadmill speed of 1.3 m/s, and for 220 s with a treadmill speed of 1.4 m/s. The first and last 10 s of all 3 datasets are discarded. To keep the bowden cable taut, and restrict any deflection of the spring to only the deflection imposed by the wearer in Figure 4.3b, the motor position was restricted as in Figure 4.3a. This restriction also makes $F_{s,\mathrm{m}} = 0$.

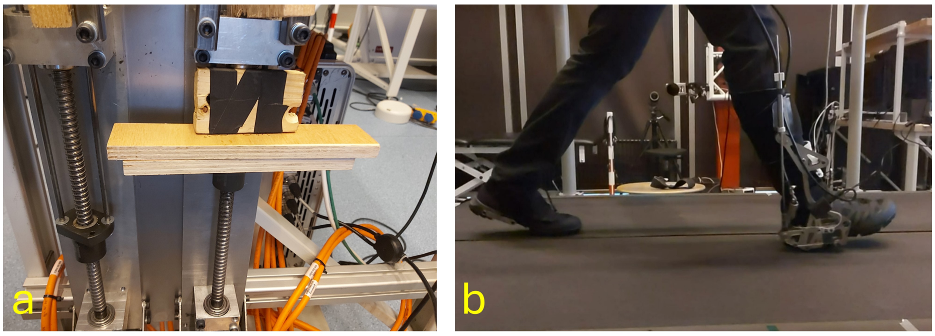

Figure 4.3: Experiment setup to determine the relationship between the load-side disturbance and the measured spring torque.(a): Physical lock to eliminate the motor as an input during the experiment. (b): Person walking on a treadmill with the JLO on their right foot.

4.2 Results of the stiffness identification

Motor-side contribution to spring torque

The polynomial model has an average normalized root mean square error (NRMSE) of 0.0294 for the estimation data. This value is 0.0295 for the validation data. The NRMSE is averaged over the five data folds. Normalization was done using the range of the measured signals (33 Nm). The parameters of the polynomial model are

$$\begin{aligned} k_1 &= 1.1713 \cdot 10^3 \text{ N/m} \\ k_2 &= 1.1622 \cdot 10^5 \text{ N/m}^2 \\ k_3 &= 4.2222 \cdot 10^6 \text{ N/m}^3 \\ k_4 &= 1.4824 \cdot 10^8 \text{ N/m}^4 \\ k_5 &= 1.3460 \cdot 10^9 \text{ N/m}^5. \end{aligned} \tag{4.7}$$

Based on these results, the lower bounds for the optimization function for the power law model are $1 \cdot 10^3$ N/m$^{p_\text{m}}$ and 1, for $k_{s,\text{m}}$, and p_m respectively. The upper bounds are $2 \cdot 10^9$ N/m$^{p_\text{m}}$ and 5, and the initial guess is $1 \cdot 10^4$ N/m$^{p_\text{m}}$ and 2. The parameters for the power law are from the fold with the lowest NRMSE. The NRMSE for the power law model is 0.0292 for both the estimation and validation data sets. This makes $k_{s,\text{m}}$ = 4.9039 · 10^4 N/m$^{p_\text{m}}$, while p_m = 1.6274. Figure 4.4 shows a comparison of the sensor data to the data estimated by both spring models.

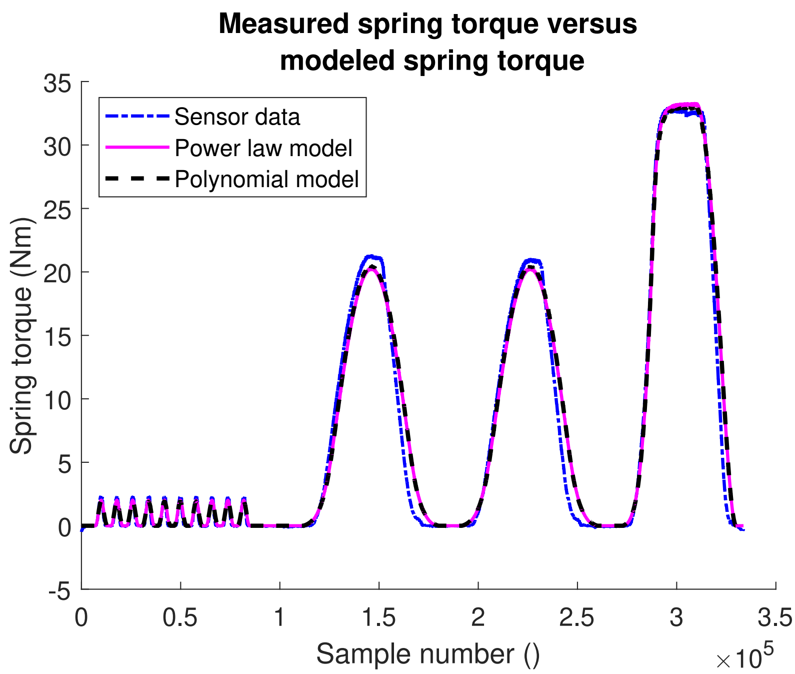

Figure 4.4: Sensor data versus the estimation of both motor-side stiffness models.

Load-side contribution to spring torque

The polynomial model has an NRMSE of 0.0634 for both the estimation and validation datasets. The NRMSE is again averaged over the five data folds. The parameters of the polynomial model are

$$\begin{aligned} k_1 &= 1.8620 \cdot 10^4 \text{ N/m} \\ k_2 &= 5.7695 \cdot 10^6 \text{ N/m}^2 \\ k_3 &= 1.1860 \cdot 10^9 \text{ N/m}^3 \\ k_4 &= 5.4640 \cdot 10^10 \text{ N/m}^4 \\ k_5 &= 1.6704 \cdot 10^9 \text{ N/m}^5. \end{aligned} \tag{4.8}$$

Based on these results, the lower bounds for the optimization function for the power law model are $1 \cdot 10^4$ N/m$^{p_\text{e}}$ and 1, for $k_{s,\text{e}}$, and p_e respectively. The upper bounds are $2 \cdot 10^9$ N/m$^{p_\text{e}}$ and 5, and the initial guess is $1 \cdot 10^4$ N/m$^{p_\text{e}}$ and 2. The parameters for the power law are from the fold with the lowest NRMSE on the estimation data, and are $k_{s,\text{e}}$ = 4.9256 · 10^5 N/m$^{p_\text{e}}$, while p_e = 1.6668. The NRMSE for the power law model is 0.0764 for the estimation data, and 0.0763 for the validation data. Figure 4.5 shows a comparison of the sensor data to the data estimated by both spring models.

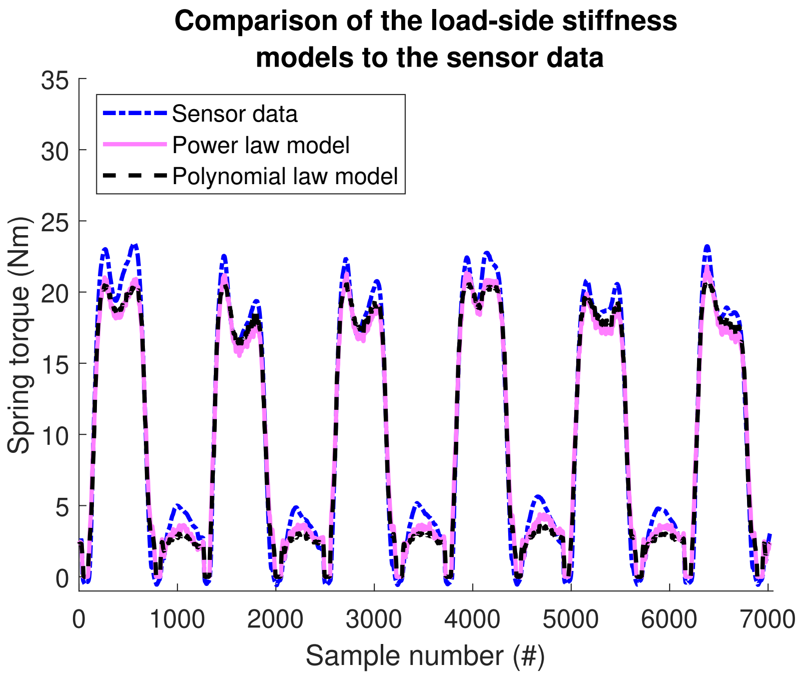

Figure 4.5: Sensor data versus the estimation of both load-side stiffness models.

Lastly, Figure 4.6 shows that the motor-side stiffness coefficients, $k_{s,\mathrm{m}}$, and p_{m} underestimate the load-side disturbance torque from the experiment shown in Figure 4.3.

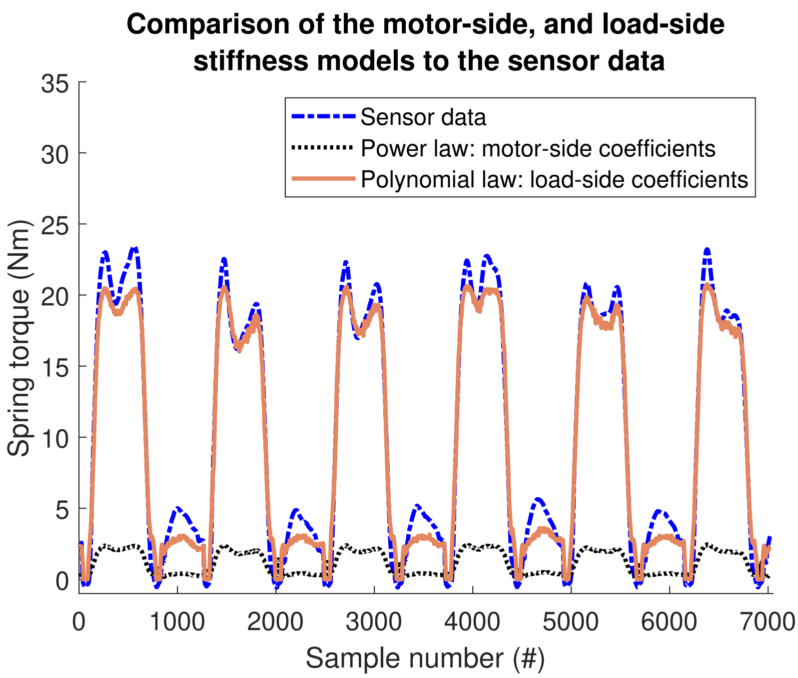

Figure 4.6: Comparison of the measured spring torque to the spring torque estimated by the motor-side spring torque model, and the load-side spring torque model

4.3 Discussion of the exoskeleton's stiffness characteristics

None of the candidate models describe a spring relationship that is based solely on physical principles. In the power law model for example, the spring constant k_s has a unit of N/m^p. Nevertheless, the power law model was chosen to describe the motor-side stiffness. This is because analytical solutions for the inverse of a power law function exist; the same cannot be said for the inverse of the 5th order polynomial. The power law model thus makes it possible to use control techniques based on model inversion to design a controller.

The polynomial model is the chosen stiffness model for the load-side stiffness, because it has a lower NRMSE than the power law model. From Figure 4.6, it is clear that the coefficients of the motor-side model do not capture the load-side torque generated by someone wearing the exoskeleton. This is likely due to the experiment design because in determining the load-side disturbance, the slack in the system was manually removed before the motor position was restricted.

Lastly, although both the power law and polynomial spring models have low relative root mean square errors, neither contains terms to explicitly account for hysteresis. A spring model that takes hysteresis into account could better characterize the torque generated by the spring. In their work, Austin et al. [20] model the nonlinear force-deflection curve with a set of piecewise linear equations. Their series elastic actuator is made from rubber; a viscoelastic material that is subject to effects such as creep and hysteresis. Modeling the JLO's stiffness with a similar model could yield a more accurate result.

Chapter 5

Controller Design and Simulation

Control hierarchies for exoskeletons often involve a high level controller that determines the desired torque, and a low level controller that enforces the demanded torque. Control system engineers employ a host of approaches in designing the low-level controllers for exoskeletons; some of these approaches include proportional-integral-derivative control (PID), impedance control, adaptive control and iterative learning.

The spring model identified in Chapter 4 is nonlinear, whereas classical feedback control is typically implemented on linear systems, or linearized systems. A linearized approximation of a nonlinear system may be obtained by applying Taylor's expansion around an equilibrium point. The disadvantage, however, of system linearization is that the controller's performance is only guaranteed in a small region around the equilibrium point [21]. Alternatively, techniques like feedback linearization, adaptive control, etc. can be used to design controllers for nonlinear systems, and the next section presents the design of a feedback linearizing controller for the JLO.

5.1 Feedback linearizing control

Feedback linearizing control involves the use of control laws that transform the nonlinear system into a linear system, thus allowing linear control design techniques to be applied. Feedback linearization allows a nonlinear affine system whose dynamics are represented by

$$\begin{aligned} \dot{x} &= f(x) + g(x)u \\ y &= h(x). \end{aligned} \tag{5.1}$$

to be transformed into a linear system by shaping the control input, u. For the JLO exoskeleton, the spring torque is modeled as the summation of the torque applied by the motor displacement, and the torque applied by the wearer

$$\begin{aligned} \hat{\tau}_s &= \hat{\tau}_{s,\mathrm{m}} - \hat{\tau}_{s,\mathrm{e}} \\ \hat{\tau}_s &= r\left(F_{s,\mathrm{m}} - F_{s,\mathrm{e}}\right). \end{aligned} \tag{5.2}$$

$F_{s,\mathrm{e}}$ is neglected in the following steps for controller design. This is because the model of the load-side disturbance, $\hat{\tau}_{s,\mathrm{e}}$, is used in a feedforward manner, and is added to the desired spring torque for compensation. This would make

$$\begin{aligned} \hat{\tau}_s^+ &= \hat{\tau}_s + \hat{\tau}_{s,\mathrm{e}} \\ \hat{\tau}_s^+ &= r k_{s,\mathrm{m}} (\lambda \theta_{\mathrm{m}}^+)^{p_\mathrm{m}}, \end{aligned} \tag{5.3}$$

Equation 5.3 explicitly denotes the addition of the compensation torque to the spring torque. The derivative of Equation 5.3 is

$$\dot{\hat{\tau}}_s^+ = \underbrace{\frac{\partial r}{\partial \theta_e} \dot{\theta}_e k_{s,\mathrm{m}} \left(\lambda \theta_m^+\right)^{p_\mathrm{m}}}_{f(x)} + \underbrace{p_\mathrm{m} r k_{s,\mathrm{m}} \left(\lambda \theta_m^+\right)^{p_\mathrm{m}-1} \lambda}_{g(x)} \underbrace{\dot{\theta}_m^+}_{u}. \tag{5.4}$$

The $f(x)$ term exists because the moment arm, r, is a function of the exoskeleton angle, and is

$$r = \frac{ab \sin(\alpha - \beta - \theta_e)}{l}. \tag{5.5}$$

The descriptions and values for the parameters in Equation 5.5 can be found in the appendix of the JLO's design document: [12].

The motor velocity bandwidth is much faster than the bandwidth of the linearizing controller, so the desired and actual motor velocity are assumed equal. Per feedback linearization, the right choice of the control input will allow linear analysis on the system. This choice often amounts to plant inversion. Based on Equation 5.4, choosing $\dot{\theta}_{m_{des}}^+$ as

$$\dot{\theta}_{m_{des}}^+ = \frac{1}{p r k_{s_m} \lambda^p \theta_{m_{des}}^{p-1}} \left(-\frac{\partial r}{\partial \theta_e} \dot{\theta}_e k_{s_m} \left(\lambda \theta_{m_{des}}^+\right)^p + v \right), \tag{5.6}$$

and substituting Equation 5.6 in Equation 5.4 makes

$$\hat{\tau}_s^+ = v, \tag{5.7}$$

where v is a control law. The JLO has a loadcell so the modeled spring torque, $\hat{\tau}_s$ is the measured spring torque, τ_s, in reality. The following control law is proposed to stabilize the system along τ_s:

$$v = \dot{\tau}_{s,\mathrm{des}} + k_p(\tau_{s,\mathrm{des}} - \tau_s). \tag{5.8}$$

The control law makes

$$\dot{\tau}_s = \dot{\tau}_{s,\text{des}} + k_p(\tau_{s,\text{des}} - \tau_s), \tag{5.9}$$

which is equivalent to

$$\dot{e}_{\tau_s} + k_p e_{\tau_s} = 0, \tag{5.10}$$

where

$$e_{\tau_s} \triangleq \tau_{s_{des}} - \tau_s. \tag{5.11}$$

k_p is the proportional gain of the controller, and Equation 5.10 is a 1st order, linear, homogeneous, differential equation that governs the evolution of the torque error. The control law stabilizes the trajectory because

$$\lim_{t\to\infty} e(t) = 0$$

regardless of the initial conditions, thus assuring global stability. The human gait cycle has a frequency of about 1 Hz [22], and because the solution to the 1st order equation governs the controller bandwidth [18], setting k_p to 62.83 should result in a controller with a bandwidth of 10 Hz which is fast enough to track changes during the gait cycle.

5.2 Simulink modeling

The controller performance is validated via simulation. The JLO is modeled in Simulink as shown in Figure 5.1. The motor's closed-loop dynamics are represented by Equation 3.11. The motor's velocity and acceleration limits are 628 rad/s, and 24678 rad/s^2, respectively. Software endstops for the motor position are at -40 rad and 90 rad. The motor contribution to the measured spring torque is represented by Equation 4.3.

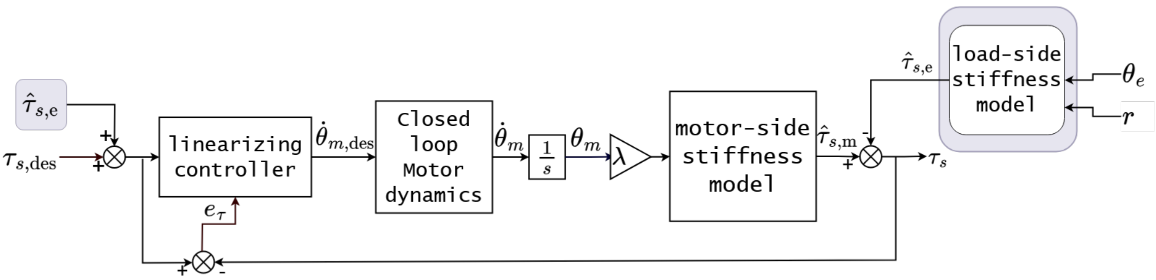

Figure 5.1: Schematic showing interconnection between the identified motor and spring models, and the feedback linearizing controller.

The exoskeleton's moment arm, r, is related to the exoskeleton angle, θ_e, using Equation 5.5. The plantarflexion-dorsiflexion data (θ_e) used in the simulation was obtained from having a participant walk on a treadmill with a treadmill speed of 1.3 m/s, and with the exoskeleton on their right foot. Figure 5.2 shows the plantarflexion-dorsiflexion angles averaged over 82 s of walking data.

For Figure 5.2, measurements from the force-instrumented treadmill were used to determine the gait phase. The gait phase has units of %; 0% coincides with initial contact, and 100% coincides with the terminal stance of of gait. Initial contact occurs when the leading foot first strikes the ground, and terminal stance occurs on the next heel strike of the same foot [23]. Positive angles represent dorsiflexion of the ankle, while negative angles represent ankle plantarflexion.

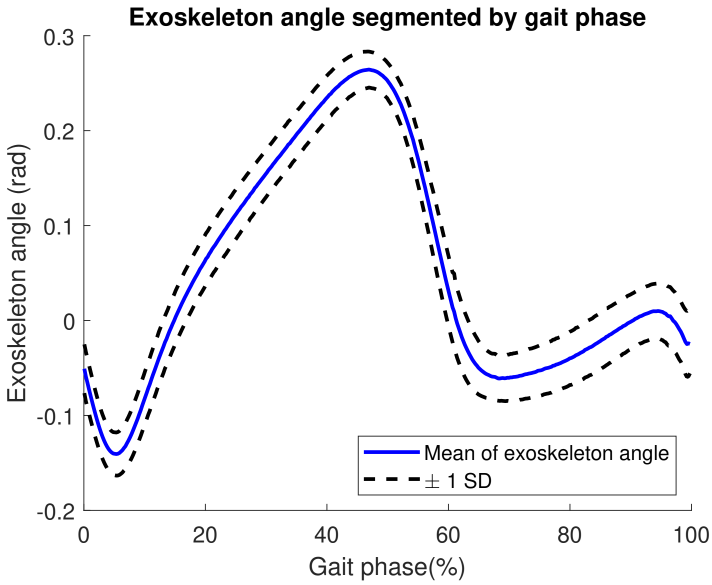

Figure 5.2: Exoskeleton angles during the gait cycle.

The desired torque pulses were the torque pulses illustrated in Figure 1.1, and given in [11]. Each pulse lasted 0.1 s, and had a period of 0.975 s, which is 0.025 s shorter than the duration of a typical gait cycle [22]. The peak torque was 10 Nm because 10 Nm is approximately 10% of the maximal ankle torque during normal walking [10].

The feedback linearizing controller given by Equations 5.6– 5.11 was modeled in Simulink. Lastly, the PD* controller was also implemented in Simulink to enable comparison with the feedback linearizing controller. Figure 5.3 shows a schematic of the PD* controller. The proportional gain of the PD* controller ($k_{p,\text{pd}}$) was 100, and the derivative gain ($k_{d,\text{pd}}$) was 0.8 as in [11], such that

$$\dot{\theta}_{\text{m,des}} = k_{p,\text{pd}} e_\tau + k_{d,\text{pd}} \dot{\theta}_{\text{m}}. \tag{5.12}$$

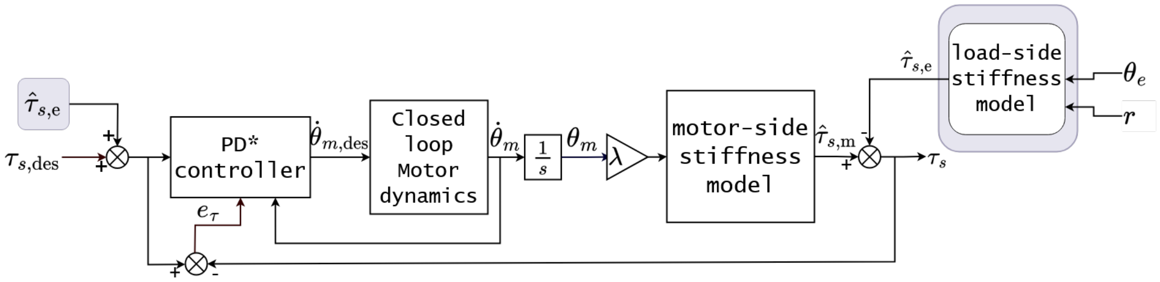

Figure 5.3: Schematic showing interconnection between the identified motor and spring models, and the PD* controller.

5.3 Results of controller design

Step responses

Figure 5.4 shows the torque tracking of both the PD* controller, and the feedforward + feedback linearizing controller, in the presence of the load-side disturbance $\hat{\tau}_{s,e}$. The data in Figure 5.4 were from a 92 s long simulation. Post simulation, the data were segmented by gait phase, and averaged to get the system response per gait phase. The RMSE for the torque tracking of the PD* controller is 0.3748 Nm, whereas that of the feedback linearizing controller is 0.1188 Nm.

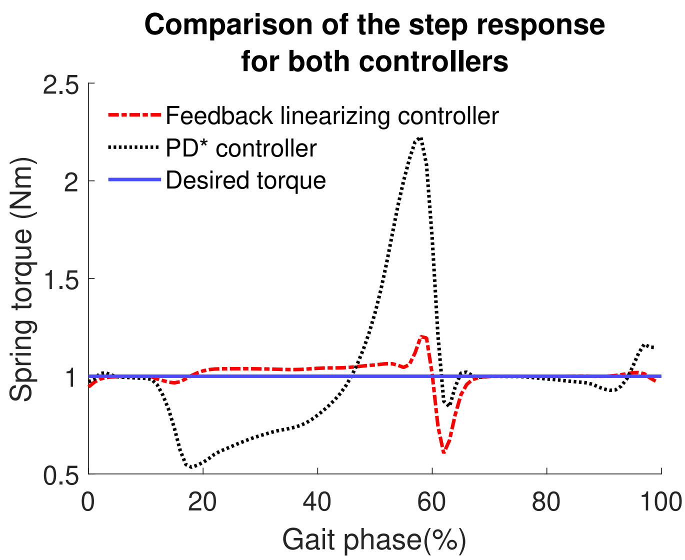

Figure 5.4: Step response of the system when it is controlled with the PD* controller, and with the feedback linearizing controller.

Figure 5.5 shows 7 s of the (unaveraged) step response data, plotted over the gait phase. The dashed lines on the plot represent an acceleration, velocity, or position limit. Unlike the position limit, the velocity and acceleration limits contribute to the degradation in torque tracking that occurs around 20% and 60% of the gait phase in Figure 5.4. The motor limits could be causing the motor to overcompensate for the increased torque error introduced by the disturbance torque. From Figures 5.4, and 5.5, it is clear that feedforward compensation anticipates the disturbance, and improves torque tracking.

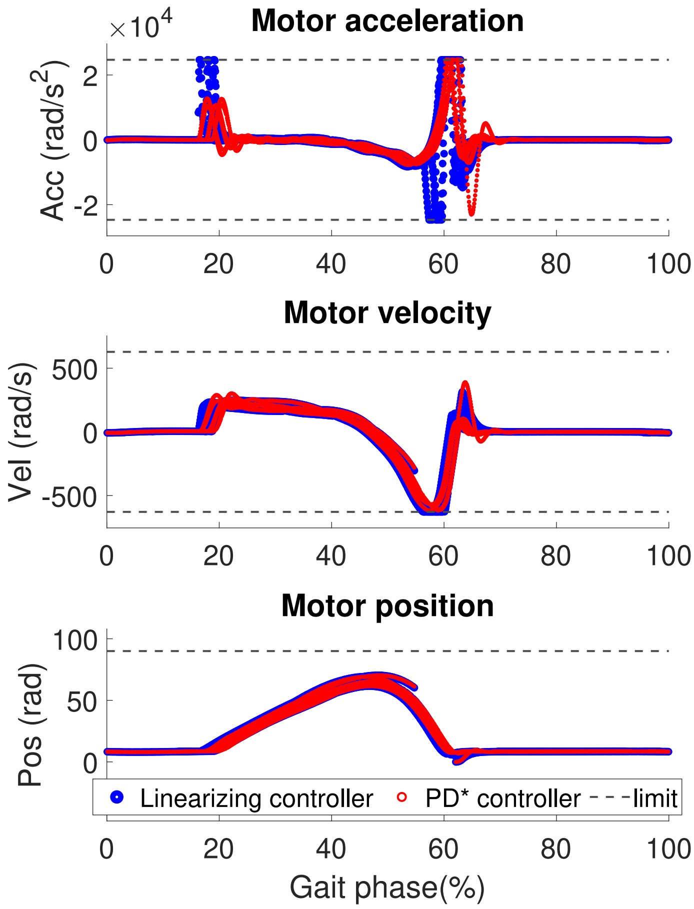

Figure 5.5: Effect of the motor's acceleration, velocity, and position limits on the step response for both controller.

Figure 5.6 shows the response to a unit step input when the JLO is controlled with the linearizing controller, and in the absence of the load-side disturbance. The rise time, which is the time it takes the system to go from 10% to 90% of the commanded signal is approximately 39 ms. A rule of thumb for the rise time, T_r, of a first order system is

$$T_r = \frac{2.2}{k_p} \text{ [18].} \tag{5.13}$$

With $k_p = 62.83$, Equation 5.13 translates to a theoretical rise time of 35 ms, making the simulated controller a close match with the theoretical one.

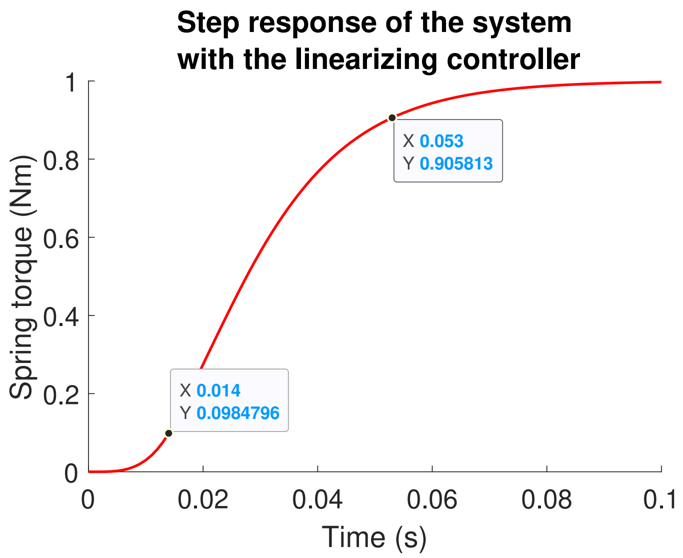

Figure 5.6: Response of the system to a step input of 1 Nm.

Pulse responses

Figure 5.7 shows the response of both controllers to a series of torque pulses that were applied throughout the gait cycle. The feedback linearizing controller has an RMSE of 0.6361 Nm, and the PD* has an RMSE of 0.7368 Nm.

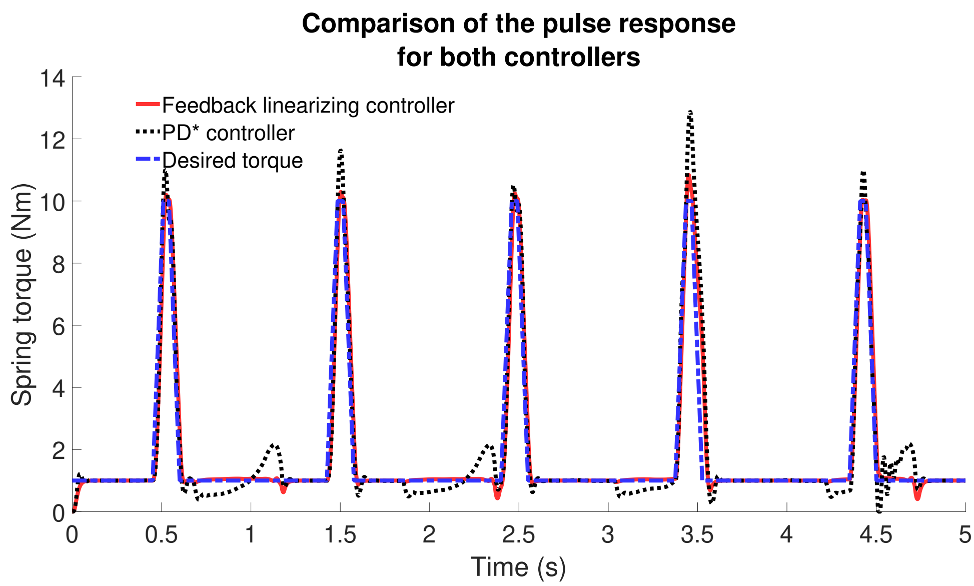

Figure 5.7: System response to torque pulses when the system is controlled with the PD* controller, and with the feedback linearizing controller.

Figure 5.8 shows the system response of the linearizing controller with, and without the compensation term for the load-side disturbance. Eliminating the compensation term for the torque generated by the wearer worsens the controller performance. The RMSE becomes 0.7295 Nm, compared to an RMSE of 0.6361 Nm when the feedforward compensation was included.

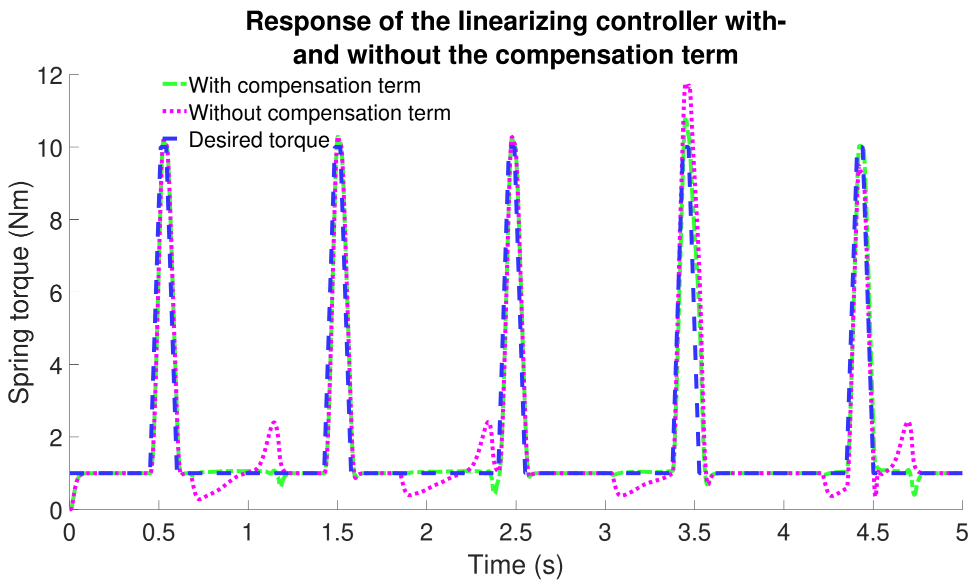

Figure 5.8: System response to torque pulses with the linearizing controller, and in the presence or absence of the compensation term $\hat{\tau}_{s_e}$.

5.4 Discussion of the controller design

The complex interplay of the motor's position, velocity, and acceleration limits affect the system response. As an example, the ankle velocity during gait peaks at pre-swing [24], which occurs around 60% of the gait cycle, and is also when the motor limits are reached, per Figure 5.5. The velocity and acceleration limits contribute to the overshooting observed in Figure 5.4, because the motor overcompensates to minimize the torque error. The motor position limits might become more apparent for users whose ankle range of motion in the sagittal plane better equals the exoskeleton's range of motion (-0.70–0.52 rad), compared to the range of angles from Figure 5.2.

The linearizing controller appears to outperform the PD* controller, an advantage that persists even in the onset of swing phase which occurs around 60% of the gait cycle [24]. The linearizing controller has a bandwidth equal to 10 Hz, making it faster than the PD* controller whose bandwidth is 8 Hz [12]. This is advantageous because higher bandwidth equals a quicker response time. However, the PD* controller gains used in this thesis resulted in an aggressive controller that seemed to outperform the JLO's actual PD* controller [11]. This could also explain why the PD* controller has a much larger overshoot in Figure 5.4, compared to the linearizing controller. However, similar to [11], this work does show that the addition of a predictive term to anticipate the load side disturbance improves the system response to torque pulses. Discrepancies between this work and [11] could be due to modeling uncertainties; the real system has the friction and hysteresis of the Bowden cable which is unmodeled in Simulink. Continuing research on the JLO should focus on creating a competent friction model, and validating the feedback linearizing controller on the real system.

Feedback linearization is a powerful technique for dealing with nonlinear systems. It allows linear controller design techniques to be used on nonlinear systems, without the need for linearizing the system around an equilibrium point. This control strategy has some disadvantages, namely its sensitivity to modeling uncertainties, and that it requires the derivative of the measured torque which could lead to noise amplification. Time constraints prevented research into other control strategies for nonlinear systems, like model reference adaptive control (MRAC) or gain scheduling. Both of these are adaptive control methods that could fare well with a less exact system model, and are suggested as a starting point for future controller design.

Chapter 6

Discussion

The first research goal of this thesis was to define a competent model for the motor powering the JLO exoskeleton. This competent model is the 2nd order transfer function given in Chapter 3, which describes the closed loop dynamics between the desired motor velocity and the actual motor velocity. Identifying a transfer function, as opposed to the parameters in the subsystems in Figure 3.1, simplified the identification process. However, the identified transfer function constrains the motor to act as a velocity source.

Switching the motor's control mode to torque mode would better facilitate the identification of a motor torque transfer function, because it would amount to identifying a transfer function using the process laid out in Chapter 3. Furthermore, the JLO's motor uses nested control, and torque control is the inner-most loop. The velocity controller is currently the outermost loop, because position control not used. Switching to torque mode would eliminate the computational time spent on the velocity loop, and could lead to a faster response from the motor.

Modeling the motor as a source of torque could also have benefits for the stiffness model, which was the second research objective. According to the instructions in [12], the motor position and the load cell force must be zeroed prior to using the JLO. A user calibrating the JLO must make the Bowden cable taut during this calibration, but this tautness is subjective. The motor-side stiffness model from Chapter 4 uses the motor position to determine the torque transmitted from the motor to the exoskeleton. The accuracy of the motor-side stiffness model thus hinges on proper calibration of the exoskeleton. A stiffness model that relates the motor torque to the spring torque should lead to results that are unaffected by calibration errors.

The power law model for the motor-side stiffness was used to fit the shape of the force-displacement plot, and does not explicitly account for hysteresis. A stiffness model like the one used in [20] uses piecewise linear functions to model a viscoelastic material, and could be a better model for describing the stiffness of the JLO. Although the power law is a simpler model than a set of linear functions, the piecewise linear functions would enable the JLO's users' to develop controllers using linear control design techniques.

For modeling the friction, the LuGre friction model was used to fit the experimental data. The motor was operated in velocity mode, which complicated further identification of the dynamic parameters of the LuGre model. Per [25] and [26], the dynamic parameters of the LuGre model are best identified with a motor that is controlled in torque mode. One reason for this is that controlling the motor in velocity mode yields noisy motor torque signals that make it difficult to determine the break away torque. Only the static friction parameters were identified in this research. The complete LuGre model is however expected to give a better fit in comparison to static models because it can capture stiction, frictional hysteresis, and stick-slip motion [27].

Unfortunately, Bowden cable systems are plagued with friction, so the accuracy of the JLO model created in this thesis is lessened in the absence of a good friction model. A good understanding of friction can lend to the design of control laws to counteract its effects. Friction models are often used to predict the motor torque that will compensate for the friction disturbance which improves torque tracking [26]. However, [28] underscored that the use of an inner position or velocity control loop, like that used in the JLO, is still advantageous when friction and backlash are large, and [16] also agreed that good velocity control still permits decent torque tracking.

On the question of compensating for the disturbance torque that a person wearing the exoskeleton introduces, Section 5.3 showed that the estimated disturbance torque improved torque tracking when used in a feed forward manner. This conforms with results from [13], and [11] who both used a model-free feed-forward compensation to improve torque tracking in their exoskeletons.

The controller designed in this thesis contributes to the advancement of gait entrainment as a rehabilitative procedure. This is because the improved torque tracking allows for a more predictable and accurate application of the desired torque pulses, and the quality of the torque control can be a limiting factor in the quality of a robot-assisted rehabilitative procedure [29].

Finally, The JLO has been in active use since 2022, so mechanical wear and tear could be affecting torque tracking. Other factors affecting the torque tracking of the JLO are the acceleration, velocity, and position limits of the motor, as well as the choice of reference signal. A reference signal with smooth, continuous derivatives is a better choice for good reference tracking. Although the desired torque pulses for the simulation experiments in Chapter 5 are trapezoidal signals, an alternative function for creating the reference signals is a logistic function because the derivative of the logistic function is continuous.

Chapter 7

Conclusions and recommendations

The goal of this thesis was to create a model-based controller that improved the torque tracking of the JLO ankle exoskeleton. Ergo, the equations of motion of the exoskeleton were detailed in Chapter 2. The motor dynamics were modeled using a 2^{nd} order transfer function in Chapter 3. The low fit error of the 2^{nd} order model made it a good representation of the motor's closed loop dynamics.

The motor model also includes position, velocity, and acceleration limits. The acceleration limit is dictated by the motor's torque limit, while the velocity limit is a safety limit imposed via software. Position limits are imposed either by the endstops of the ball screw transmission or the dorsiflexion-plantarflexion range of motion of the person donning the exoskeleton. These limits influence the JLO's ability to deliver the desired torque pulses, as is shown in Chapter 5. The motor's torque limit is set to 2.85 Nm and is lower than the nominal torque of 3 Nm. There is less room for adjusting the motor's velocity limit, but adjusting the torque limit is an accessible improvement could better torque tracking

The model of the JLO is a novel contribution of this thesis. In Chapter 3, the motor was modeled as a velocity source, and the system stiffness was modeled with nonlinear equations that relate the measured spring torque to the motor position and the exoskeleton angle in Chapter 4. The stiffness model does not account for hysteresis so updates to the stiffness model can use the work of Austin et al. [20] as inspiration. They model a series elastic actuator using piecewise linear equations that encode hysteresis.

Chapter 5 showcases the results of designing a feedback linearizing controller for the exoskeleton. The identified spring models in Chapter 4 are nonlinear, hence feedback linearization was used in designing the controller. The designed controller has a bandwidth of 10 Hz, compared to 8 Hz of the JLO's current PD* controller.

Simulation experiments also show that the new controller provides more consistent torque pulses across the gait cycle unlike the PD* controller. Combining the linearizing controller with a feedforward term to compensate for the disturbance torque generated by the human results in a lower RMSE than the linearizing controller solely achieves.

To conclude, future work on the JLO could include updating the software safety architecture to make torque control of the motor a viable option, and updating the motor's torque limit. It is also a good idea that any future redesigns of the exoskeleton make the calibration of the JLO less prone to human error.

Bibliography

[1] S. Dattani, L. Rodés-Guirao, H. Ritchie, E. Ortiz-Ospina, and M. Roser, "Life expectancy," *Our World in Data*, 2023, https://ourworldindata.org/life-expectancy.

[2] F. Pieruccini-Faria, S. E. Black, M. Masellis, E. E. Smith, Q. J. Almeida, K. Z. Li, L. Bherer, R. Camicioli, and M. Montero-Odasso, "Gait variability across neurodegenerative and cognitive disorders: Results from the canadian consortium of neurodegeneration in aging (ccna) and the gait and brain study," *Alzheimer's & Dementia*, vol. 17, no. 8, pp. 1317–1328, 2021.

[3] C. Lagoda, A. C. Schouten, A. H. A. Stienen, E. E. G. Hekman, and H. van der Kooij, "Design of an electric series elastic actuated joint for robotic gait rehabilitation training," in *2010 3rd IEEE RAS EMBS International Conference on Biomedical Robotics and Biomechatronics*, 2010, pp. 21–26.

[4] R. S. Calabrò, A. Manuli, A. Leo, M. Russo, A. Naro, and P. Bramanti, "Gait rehabilitation following neurological disorders: are robotic devices the future?" *Innovations in Clinical Neuroscience*, vol. 15, no. 09-10, p. 11, 2018.

[5] F. Giorgi, D. Donati, and R. Tedeschi, "Cueing interventions for gait and balance in parkinson's disease: A scoping review of current evidence," *Applied Sciences*, vol. 14, no. 24, p. 11781, 2024.

[6] E. Sejdic, Y. Fu, A. Pak, J. Fairley, and T. Chau, "The effects of rhythmic sensory cues on the temporal dynamics of human gait," *PloS one*, vol. 7, p. e43104, 08 2012.

[7] G. C. McIntosh, S. H. Brown, R. R. Rice, and M. H. Thaut, "Rhythmic auditory-motor facilitation of gait patterns in patients with parkinson's disease." *Journal of Neurology, Neurosurgery & Psychiatry*, vol. 62, no. 1, pp. 22–26, 1997.

[8] G. D. Hayward, "Let's walk and talk': The effect of social interaction on gait entrainment," *Unpublished master's thesis]. University of Cambridge*, 2009.

[9] J. Ahn, T. Patterson, H. Lee, D. Klenk, A. Lo, H. I. Krebs, and N. Hogan, "Feasibility of entrainment with ankle mechanical perturbation to treat locomotor

deficit of neurologically impaired patients," in *2011 Annual International Conference of the IEEE Engineering in Medicine and Biology Society*, 2011, pp. 7474–7477.

[10] J. Ahn and N. Hogan, "Walking is not like reaching: evidence from periodic mechanical perturbations," *PloS one*, vol. 7, no. 3, p. e31767, 2012.

[11] Z. S. Mahdian, H. van der Kooij, and M. K. MacLean, "Iterative learning compensation control for torque tracking of short pulses throughout gait cycle with an ankle exoskeleton," in *2024 10th IEEE RAS/EMBS International Conference for Biomedical Robotics and Biomechatronics (BioRob)*, 2024, pp. 1802–1808.

[12] J. Meijners, "The design, control, and integration of a bowden cable actuation for an ankle exoskeleton," Master's thesis, University of Twente, Enschede, The Netherlands, June 2022.

[13] J. Zhang, C. C. Cheah, and S. H. Collins, "Torque control in legged locomotion," in *Bioinspired Legged Locomotion*. Elsevier, 2017, pp. 347–400.

[14] M. Eveld, E. van Asseldonk, and H. van der Kooij, "A disturbance-cancelling approach for ankle exoskeleton assistance improves standing balance performance and reduces human effort," in *2024 10th IEEE RAS/EMBS International Conference for Biomedical Robotics and Biomechatronics (BioRob)*, 2024, pp. 1549–1554.

[15] Y. Shi, M. Guo, C. Hui, S. Li, X. Ji, Y. Yang, X. Luo, and D. Xia, "Learning-based repetitive control of a bowden-cable-actuated exoskeleton with frictional hysteresis," *Micromachines*, vol. 13, no. 10, p. 1674, 2022.

[16] G. Wyeth, "Control issues for velocity sourced series elastic actuators," in *Proceedings of the 2006 Australasian Conference on Robotics and Automation*. Australian Robotics and Automation Association, 2006, pp. 1–6.

[17] D. W. Robinson, "Design and analysis of series elasticity in closed-loop actuator force control," 2000. [Online]. Available: https://api.semanticscholar.org/CorpusID:6987466

[18] N. S. Nise, *Control systems engineering*. John Wiley & Sons, 2020.

[19] J. Pachouly, S. Ahirrao, K. Kotecha, G. Selvachandran, and A. Abraham, "A systematic literature review on software defect prediction using artificial intelligence: Datasets, data validation methods, approaches, and tools," *Engineering Applications of Artificial Intelligence*, vol. 111, p. 104773, 2022.

[20] J. Austin, A. Schepelmann, and H. Geyer, "Control and evaluation of series elastic actuators with nonlinear rubber springs," in *2015 IEEE/RSJ International Conference on Intelligent Robots and Systems (IROS)*. IEEE, 2015, pp. 6563–6568.

[21] D. H. Nguyen, M. H. Lowenberg, and S. A. Neild, "Identifying limits of linear control design validity in nonlinear systems: a continuation-based approach," *Nonlinear Dynamics*, vol. 104, no. 2, pp. 901–921, 2021.

[22] S. Scataglini, S. Verwulgen, E. Roosens, R. Haelterman, and D. Van Tiggelen, "Measuring spatiotemporal parameters on treadmill walking using wearable inertial system," *Sensors*, vol. 21, no. 13, p. 4441, 2021.

[23] W. Tao, T. Liu, R. Zheng, and H. Feng, "Gait analysis using wearable sensors," *Sensors*, vol. 12, no. 2, pp. 2255–2283, 2012.

[24] G. Williams, B. F. Mentiplay, M. B. Kahn, R. A. Clark, and M. Banky, "The effect of walking speed on lower limb angular velocity," *Archives of Physical Medicine and Rehabilitation*, vol. 99, no. 10, pp. e12–e13, 2018.

[25] P. Lischinsky, C. Canudas-de Wit, and G. Morel, "Friction compensation for an industrial hydraulic robot," *Control Systems, IEEE*, vol. 19, pp. 25 – 32, 03 1999.

[26] C. C. De Wit and P. Lischinsky, "Adaptive friction compensation with partially known dynamic friction model," *International journal of adaptive control and signal processing*, vol. 11, no. 1, pp. 65–80, 1997.

[27] H. Olsson, K. J. Åström, C. C. De Wit, M. Gäfvert, and P. Lischinsky, "Friction models and friction compensation," *Eur. J. Control*, vol. 4, no. 3, pp. 176–195, 1998.

[28] N. Paine, J. S. Mehling, J. Holley, N. A. Radford, G. Johnson, C. Fok, and L. Sentis, "Actuator control for the nasa-jsc valkyrie humanoid robot: A decoupled dynamics approach for torque control of series elastic robots," *Journal of Field Robotics*, vol. 32, no. 3, p. 378–396, Jan 2015.

[29] C. Lagoda, A. C. Schouten, A. H. Stienen, E. E. Hekman, and H. van der Kooij, "Design of an electric series elastic actuated joint for robotic gait rehabilitation training," in *2010 3rd IEEE RAS & EMBS international conference on biomedical robotics and biomechatronics*. IEEE, 2010, pp. 21–26.

[30] M. Dežman, T. Asfour, A. Ude, and A. Gams, "Mechanical design and friction modelling of a cable-driven upper-limb exoskeleton," *Mechanism and Machine Theory*, vol. 171, p. 104746, 2022.

[31] V. Agrawal, W. J. Peine, and B. Yao, “Modeling of transmission characteristics across a cable-conduit system,” *IEEE Transactions on Robotics*, vol. 26, no. 5, pp. 914–924, 2010.

[32] U. Jeong and K.-J. Cho, “Control of a bowden-cable actuation system with embedded boasensor for soft wearable robots,” *IEEE Transactions on Industrial Electronics*, vol. 67, no. 9, pp. 7669–7680, 2019.

Appendix A

Artificial Intelligence (AI) statement

During the preparation of this work, I used no artificial intelligence tools.

Appendix B

Friction modeling

Using compliant elements like Bowden cables in series with a drive system is a proven strategy for improving torque tracking in exoskeletons. This strategy can help to minimize effects such as backlash in the gearbox or cogging, although this comes with a loss of bandwidth [3]. Bowden cables, specifically, allow the motor to be relocated which results in a reduction of the exoskeleton inertia. However, the downside of adding a Bowden cable is that its complex friction profile can prove an additional challenge for control of the exoskeleton, especially when the Bowden cable is kept slack [13].

Dežman et al. [30] expounded on the complexities of including a Bowden cable in the mechanical design of an exoskeleton, due to its difficult-to-characterize friction properties. To describe the bowden cable friction, they compared the Stribeck + Coulomb + Viscous (SCV) friction model variant with a second model variant. The second variant included terms to account for any adhesive behavior between the Bowden cable and the Bowden sheath, and showed a 15% better fit to experimental data than the original SCV model [30].

Agrawal et al. [31] also conducted research on the nonlinearities introduced by the Bowden cable, and the importance of accurate modeling of the Bowden cable. In their work, they focused on Bowden cables that are used in pairs, a configuration that is common in surgical robotics. To that end, they propose a set of differential equations to describe the motion and power transmission characteristics of Bowden cables used in a pull-pull configuration.

Furthermore, Jeong and Cho [32] reported on how the frictional nonlinearity of the Bowden cable varies as the bend angle changes. They proposed a model based on the Capstan equation augmented with an extra term to account for the inherent efficiency of the cable.

Unlike the previously-discussed static friction models, the LuGre model is a dynamic friction model that is capable of describing complex friction behavior including stick-slip motion, Stribeck effects, and frictional lag. Although friction is often modeled using static equations, dynamic models can better explain effects like frictional lag or stick slip behavior [26], and the LuGre model was used to fit experimental data.

The parameters of the LuGre friction model may be divided in two categories, where the first category contains a set of four static parameters that map the steady state velocity to the friction force. This makes the static part of the LuGre model similar to the SCV model from [30]. The second set of parameters describe the dynamic friction response [25].

The descriptive equations for the LuGre model are given below.

$$\frac{dz}{dt} = \dot{q} - \frac{\sigma_0}{g(\dot{q})} z|\dot{q}|, \quad g(\dot{q}) = \alpha_0 + \alpha_1 e^{-\frac{q}{v_0}^{2}}, \tag{B.1}$$

$$F = \sigma_0 z + \sigma_1 \frac{dz}{dt} + \alpha_2 \dot{q}. \tag{B.2}$$

$\dot{q}$ is the angular velocity, and F is the friction torque. Equation B.1 captures the internal friction dynamics, although the state z is unmeasurable. Furthermore, the steady state friction characteristics are given by

$$F_{ss} = \left(\alpha_0 + \alpha_1 e^{-\frac{q}{v_0}^{2}}\right) sgn(\dot{q}) + \alpha \dot{q}, \tag{B.3}$$

Table B.1: Relevant parameters for describing the LuGre friction model

Symbol	**Description**	**Unit**
$\dot{q}$	Velocity	$\frac{m}{s}$
z	Friction internal state	m
σ_0	Dynamic friction parameter	$\frac{N}{m}$
$g(\dot{q})$	A function which describes part of the friction for constant velocity inputs	N
α_0	Coulomb friction	N
α_1	Static friction parameter	N
v_0	Stribeck velocity	$\frac{m}{s}$
α_2	Viscous friction term	$\frac{Ns}{m}$

B.1 Process for identifying the frictional properties of the exoskeleton

The exoskeleton was excited using a series of constant velocity signals with amplitudes of 0.1,0.2, 0.5, 1, 5, and 10 rad/s shown in Figure B.1.

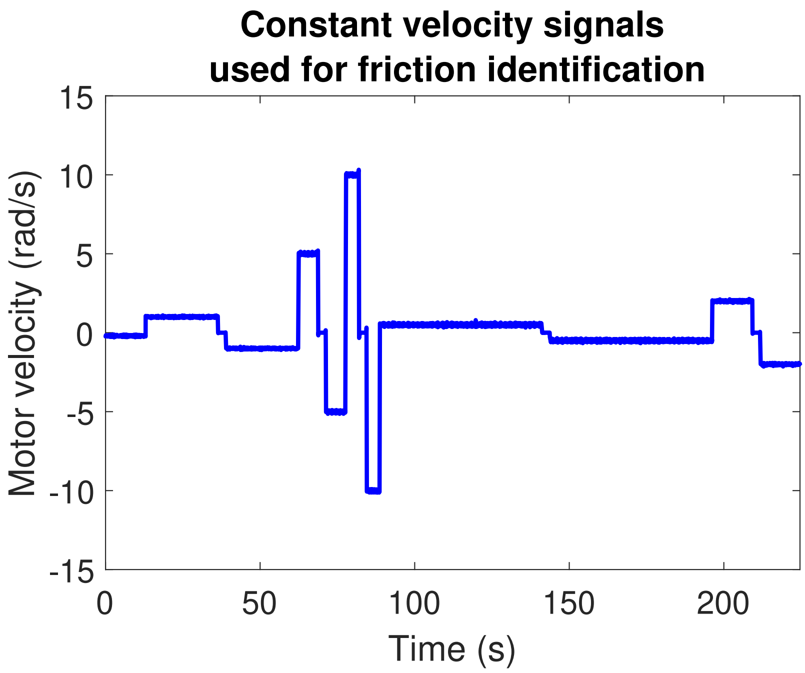

Figure B.1: Constant velocity data used for the identification of friction parameters

The constant velocity signals mean that the acceleration terms vanish. Also, the spring and Bowden cable masses are considered negligible, so the equation used for the identification process thus simplifies from Equation 2.4 to

$$\tau_m(t) = B_c\dot{\theta}_m(t) + \lambda\left(F_s + F_f(t)\right). \tag{B.4}$$

Rewriting Equation B.4 gives

$$\frac{\tau_m(t)}{\lambda} - F_s = B_c\dot{\theta}_m(t) + F_f(t) \tag{B.5}$$

The term $B_c\dot{\theta}_m(t)$ is lumped into the term $\alpha\dot{q}$ in Equation B.3 because both terms describe viscous friction, so combining them should improve the accuracy of the estimation. Thus, the equation relating the motor torque to the friction is

$$F_f(t) = \frac{\tau_m(t)}{\lambda} - F_s = \left(\alpha_0 + \alpha_1 e^{-\frac{q}{v_0}^2}\right)\text{sgn}(\dot{q}) + \alpha\dot{q}. \tag{B.6}$$

Similar to Section 4.1, the data are filtered in the forward and reverse directions with the low-pass filter whose coefficients are given in Equation 4.1. The coefficients in the static part of the LuGre model are determined using MATLAB's *fmincon* optimization routine. The error function, e, and the objective for the optimization, P, are

$$e = \frac{\tau_m(t)}{\lambda} - F_s - \left(\alpha_0 + \alpha_1 e^{-\frac{q}{v_0}^2}\right) \text{sgn}(\dot{q}) - \alpha\dot{q} \tag{B.7}$$

$$P = \frac{1}{N} e \cdot e, \text{ respectively.} \tag{B.8}$$

The data were split into 5 folds for k-fold cross validation. The lower bounds and initial guesses for all parameters were set to 0 and 1 respectively. The upper bounds for all parameters besides v_0 was 100. The upper bounds for v_0 was 1 m/s.

B.2 Results and discussion of friction identification

The static parameters identified for the LuGre friction model are

$$\begin{aligned} \alpha_0 &= 30 \text{ N} \\ \alpha_1 &= 29 \text{ N} \\ \alpha_2 &= 14.15 \text{ Ns/m} \\ v_0 &= 0.54 \text{ m/s.} \end{aligned} \tag{B.9}$$

The static model has an NRMSE of 0.1368 for the estimation data, and 0.1362 for the validation data. From is apparent that the bowden cable friction cannot be accurately described by a static model. In research, the dynamic parameters of the LuGre model were estimated by exciting the system using open loop torque signals that were smaller than the brekaway torque [26]. This was difficult to replicate in the JLO as the motor is operated in velocity mode, and trying to obtain torque signals using velocity commands results in noisy output.

Treating the motor as a torque source makes it easier to quantify the effects of friction. Wyeth [16] posits a well tuned velocity controller should be able to deal with low-frequency torque disturbances, even in the presence of significant coulomb and viscous friction losses in the motor and in the gearbox. As the motor is treated as a velocity source, the friction model is not further considered in this research.

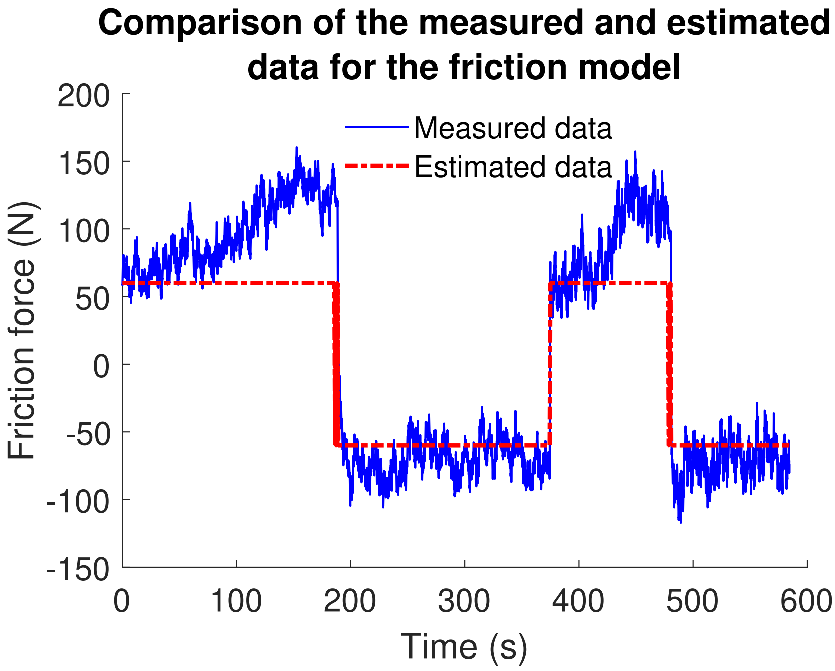

Figure B.2: Results of the identification of parameters of the dynamic LuGre friction model.

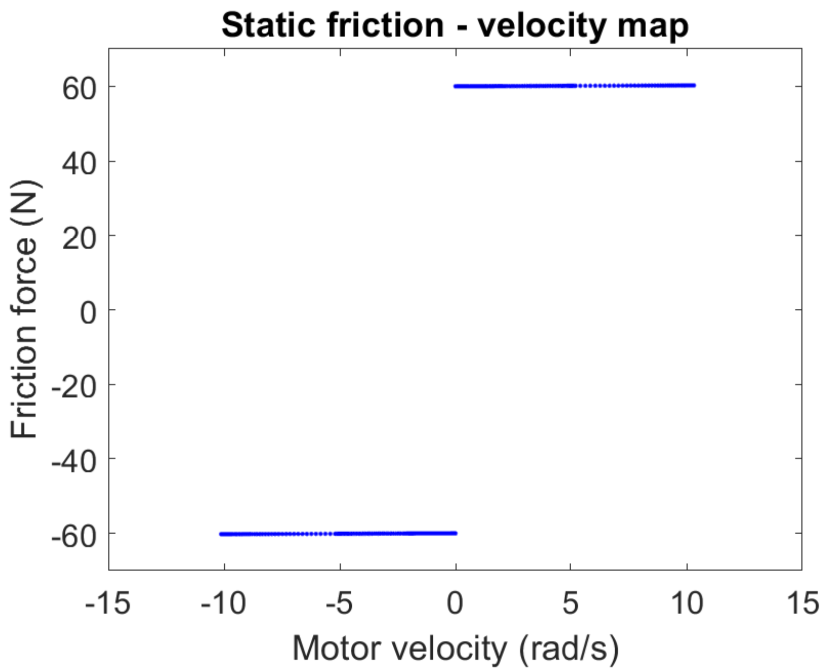

Figure B.3: Static friction map for the JLO.